Hyperboloid Structures Formed by Polarization Singularities in Coherent Vector Fields with Longitudinal-Transverse Coupling

Y. F. Chen,* T. H. Lu, and K. F. Huang

Department of Electrophysics, National Chiao Tung University, Hsinchu Taiwan

(Received 3 July 2006; published 7 December 2006)

The propagation-dependent polarization vector fields are experimentally created from an isotropic microchip laser with a longitudinal-transverse coupling and entanglement of the polarization states. The experimental three-dimensional coherent vector fields are analytically reconstructed with a coherent superposition of orthogonal circularly polarized vortex modes. Each polarized component is found to comprise two Laguerre-Gaussian modes with different topological charges. With the analytical representation, the polarization singularities, on which the electric polarization ellipse is purely circular (*C* lines) or purely linear (*L* surfaces), are explored. The *C* line singularities are found to form an intriguing hyperboloidal structure.

DOI: 10.1103/PhysRevLett.97.233903 PACS numbers: 42.25.Ja, 02.40.Xx, 03.65.Vf, 42.60.Jf

Phase singularities in complex scalar waves, known as vortices and edge dislocations, play an important role in a vast variety of coherent phenomena such as linear and nonlinear optics [1,2], quantum and microwave billiards [3], superconducting films [4], Bose-Einstein condensates [5], quantum ballistic transport [6], and liquid crystal films [7]. In addition to phase singularities, the vector nature of light can support the most complicated type of singularities, known as polarization singularities and wave front disclinations [8]. A special case of polarization singularities is vector singularities (*V* points), which are isolated, stationary points at which the orientation of the electric vector of a linearly polarized vector field becomes undefined. However, the more general state of the optical field with two orthogonal components is elliptically polarized not linearly polarized. The elliptically polarized vector field maintains two types of generic singularities [9]: *C* lines, on which the field is circularly polarized and the orientations of the major and minor axes of the ellipse are undefined, and *L* surfaces, on which the field is linearly polarized and the handedness of the ellipse becomes undefined. In the observation plane, *C* lines and *L* surface present as *C* points and *L* lines, respectively. Note that *L* surfaces exist only in paraxial fields; in fully three-dimensional fields these surfaces generally become *L* lines and they are points in the observation plane [10]. The underlying polarization singularities of elliptically polarized fields have been confirmed in detail by experiments with microwaves [9] and optical waves [11]. Recently, the complicated *V* point structure has been manifested from the observations of low-order [12] and high-order [13] space-dependent linearly polarized fields in transversely isotropic lasers.

In this Letter we originally create the propagation-dependent polarization vector fields from an isotropic microchip laser with the longitudinal-transverse coupling and the entanglement of the polarization states. With the theoretical wave representation, the characteristics of *V* point, *C* line, and *L* surface singularities are systematically analyzed. It is found that the *C* line singularities organize a hyperboloidal structure.

In this experiment, the laser cavity was formed by a spherical mirror and a gain medium. The spherical mirror was a 10-mm radius-of-curvature concave mirror with antireflection coating at the pumping wavelength on the entrance face ($R < 0.2\%$), high-reflection coating at lasing wavelength ($R > 99.8\%$), and high-transmission coating at the pumping wavelength on the other surface ($T > 95\%$). The gain medium was a 2.0 at. % Nd: YVO_4 crystal with the length of 2 mm. The laser crystal was precisely cut along the *c* axis for high-level transverse isotropy [13]. One planar surface of the laser crystal was coated for antireflection at the pumping and lasing wavelengths; the other surface was coated to be an output coupler with the reflectivity of 99%. The pump source was a 1-W 808-nm fiber-coupled laser diode with a core diameter of 100 μm and a numerical aperture of 0.2. A focusing lens was used to reimage the pump beam into the laser crystal. The pump spot radius, w_p, was controlled to be in the range of 50–200 μm. The effective cavity length was set in the range of 9.6–9.9 mm to form a nearly hemispherical resonator, in which the fundamental cavity mode size, w_0, was approximately 20 μm. Since the pump-to-mode size ratio was significantly greater than unity, a variety of high-order transverse modes could be generated. The Fresnel number for the end-pumped lasers can be expressed as $\mathrm{Fr} = w_p^2/(\pi w_0^2)$. Consequently, the Fresnel number in the experiment can be varied from 2 to 30.

To measure the far-field pattern, the output beam was directly projected on a paper screen at a distance of $\sim$50 cm from the rear cavity mirror and the scattered light was captured by a digital camera. Figures 1(a)–1(d) show four experimental far-field transverse patterns near lasing threshold measured at different pump-to-mode size ratios. The far-field patterns have intensity distributions like LG flowers modes with single or multiple rings. The funda-

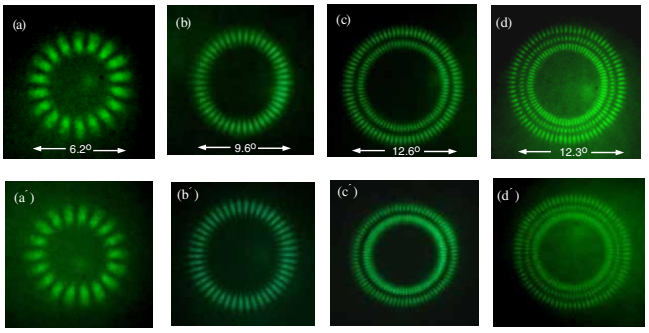

FIG. 1 (color online). Experimental far-field transverse patterns measured at different pump-to-mode size ratios: (a) $w_p/w_0 = 3.2$, Fr = 3.3; (b) $w_p/w_0 = 4.9$, Fr = 7.6; (c) $w_p/w_0 = 6.3$, Fr = 12.6; (d) $w_p/w_0 = 6.7$, Fr = 14.3; (a′)–(d′): experimental transverse patterns at the beam waist.

mental mode is not excited due to the fact that its lasing threshold is higher than that of high-order transverse modes in the present pump distribution. As shown in Figs. 1(a′), 1(b′), 1(c′), and 1(d′), the intensity distributions at the beam waist remain almost the same as the far-field patterns, except for a rotation of an angle. However, the tomographic and polarization-resolved transverse patterns reveal the lasing modes to be the salient three-dimensional (3D) coherent vector fields. A microscope objective lens mounted on a translation stage was used to reimage the tomographic transverse patterns at different propagation positions onto a CCD camera. Figure 2 shows the polarization-resolved transverse patterns for the experimental result depicted in Fig. 1(b) at three different propagation positions: $z = 0$, $z = z_R$, and $z \gg z_R$, where Z_R is the Rayleigh range and $Z_R = 1.26$ mm. It can be seen that the polarization state behaves like an azimuthally polarized flower mode at the beam waist ($z = 0$), whereas it turns to be like a radially polarized flower mode in the far field ($z \gg Z_R$). On the other hand, a quarter-wave plate was used to confirm that the polarization state at $z = z_R$ behaves like a circularly polarized flower mode. To be precise, the lasing modes are propagation-dependent polarization vector fields. The following analysis will verify that the formation of 3D coherent vector fields arises from the longitudinal-transverse coupling with the entanglement of the polarization states.

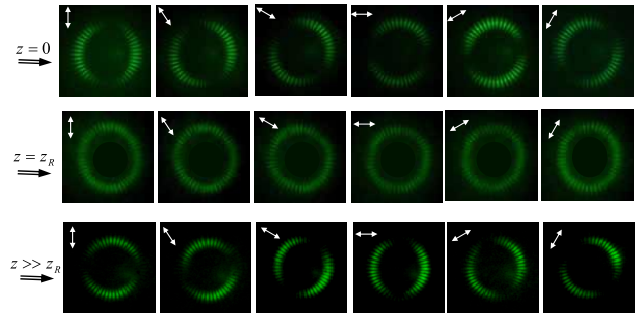

FIG. 2 (color online). Polarization-resolved transverse patterns for the experimental result depicted in Fig. 1(b) at three different propagation positions: $z = 0$, $z = z_R$, and $z \gg z_R$, where $Z_R = 1.26$ mm. The arrows indicate the transmission axis of the polarizer.

The wave function of LG mode with longitudinal index s, transverse radial index p, and transverse azimuthal index l in cylindrical coordinates (ρ, ϕ, z) is given by $\Psi_{p,l,s}(\rho, \phi, z) = e^{il\phi}\Phi_{p,l,s}(\rho, z)$, where

$$\Phi_{p,l,s}(\rho, z) = \sqrt{\frac{2p!}{\pi(p+|l|)!}}\frac{1}{w(z)}\left(\frac{\sqrt{2}\rho}{w(z)}\right)^{|l|} L_p^{|l|}\left(\frac{2\rho^2}{w(z)^2}\right) \times \exp\left[-\frac{\rho^2}{w(z)^2}\right]\exp\left\{-ik_{p,l,s}z\left[1 + \frac{\rho^2}{2(z^2+z_R^2)}\right]\right\}\exp[i(2p+|l|+1)\theta_G(z)], \tag{1}$$

where $w(z) = w_0\sqrt{1+(z/z_R)^2}$, w_0 is the beam radius at the waist, and $z_R = \pi w_0^2/\lambda$ is the Rayleigh range, $L_p^l(\cdot)$ are the associated Laguerre polynomials, $k_{p,l,s}$ is the wave number, and $\theta_G(z) = \tan^{-1}(z/z_R)$ is the Gouy phase. In terms of the effective length L, the wave number $k_{p,l,s}$ is given by $k_{p,l,s}L = \pi[s + (2p + |l|)(\Delta f_T/\Delta f_L)]$, where $\Delta f_L = c/2L$ is the longitudinal mode spacing and Δf_T is the transverse mode spacing. It has been evidenced [14] that when the ratio $\Delta f_T/\Delta f_L$ is close to a simple fractional, the longitudinal-transverse coupling usually brings about the frequency locking among different transverse modes with the help of different longitudinal orders. For the present cavity configuration, $\Delta f_T/\Delta f_L \approx 1/2$, the group of the LG modes $\Psi_{p,l+2k,s-k}(\rho, \phi, z)$, with $k = 0, 1, 2, 3, \ldots$, forms an important family of frequency degenerate states.

The experimental polarization-resolved patterns indicate that the 3D electric vector fields at $z = 0$ and $\rho = \rho_{\max}$ can be described as the equation: $|E\rangle \propto (-\sin\phi|x\rangle + \cos\phi|y\rangle)\sin(l\phi)$, where $|x\rangle = (1, 0)^T$, $|y\rangle = (0, 1)^T$, the superscript T denotes a vector superposition, and $\rho_{\max}$ is the transverse radius of maximum intensity. With LG modes as a basis, the experimental vector fields can be decomposed into a coherent superposition of orthogonal circularly polarized helical modes $|E\rangle = E_R(\rho, \phi, z)|R\rangle + E_L(\rho, \phi, z)|L\rangle$, where

$$E_R(\rho, \phi, z) = [\Psi_{p,-(l+1),s-1}(\rho, \phi, z) - \Psi_{p,l-1,s}(\rho, \phi, z)]/\sqrt{2}, \tag{2}$$

$$E_L(\rho, \phi, z) = [\Psi_{p,l+1,s-1}(\rho, \phi, z) - \Psi_{p,-(l-1),s}(\rho, \phi, z)]/\sqrt{2}, \tag{3}$$

and $|R\rangle = (1, i)^T/\sqrt{2}$ and $|L\rangle = (1, -i)^T/\sqrt{2}$ are the helical basis unit vectors for the right- and left-handed circulation polarizations, respectively. Figure 3 depicts the numerically reconstructed patterns for the experimental

results shown in Fig. 2. The good agreement between the reconstructed and experimental patterns confirms that the circularly polarized vortex modes form an important basis for describing the propagation-dependent polarization vector fields. It is worth noting that the circularly polarized vortex modes are also the important eigenmodes for the spin-orbit interaction in a multimode fiber [15]. Equations (2) and (3) indicate that each circularly polarized component of the vector fields is made up of two LG modes with different topological charges. The frequency locking of two LG modes with different azimuthal orders comes from the longitudinal-transverse coupling in a nearly hemispheric cavity, as mentioned earlier.

For simplicity, we consider the case of $p = 0$ to analyze the trajectories of C line singularities. After some algebra, Eqs. (2) and (3) for $p = 0$ can be simplified as

$$E_R(\rho, \phi, z) = [\tilde{\rho}_l^2 e^{-i2l\phi} e^{i2\theta_G(z)} - 1] e^{i(l-1)\phi} \Phi_{0,l-1,s}(\rho, z)/\sqrt{2}, \quad (4)$$

$$E_L(\rho, \phi, z) = [\tilde{\rho}_l^2 e^{i2l\phi} e^{i2\theta_G(z)} - 1] e^{-i(l-1)\phi} \Phi_{0,l-1,s}(\rho, z)/\sqrt{2}, \quad (5)$$

where $\tilde{\rho}_l^2 = [\sqrt{2}\rho/w(z)]^2[1/\sqrt{l(l+1)}]$. In the basis of circular polarizations, the conditions for left-handed and right-handed C point loci can be given by $E_R(\rho, \phi, z) = 0$ and $E_L(\rho, \phi, z) = 0$, respectively. For the paraxial 3D vector fields, the trajectories of C singularities can be expressed as the parametric curves with z as a variable. In addition to the central singularity at the origin, the expression in the bracket of Eq. (4) indicates the left-handed C point trajectories are determined by the two equations: $\tilde{\rho}_l^2 = 1$ and $e^{-i2l\phi} e^{i2\theta_G(z)} = 1$. As a result, there are $2l$ peripheral left-handed C points symmetrically arrayed on a circle of radius $\rho_0 = \sqrt{\sqrt{l(l+1)}} w(z)/\sqrt{2}$ at angles $\phi_m = [\theta_G(z) + m\pi]/l$ with $m = 0, 1, 2, \ldots, 2l - 1$. Note that the radius ρ_0 coincides with the radial position of maximum intensity $\rho_{\max}$. In the same way, Eq. (5) implies that there are $2l$ peripheral right-handed C points on a circle of radius ρ_0 at angles $\phi_m = (-\theta_G(z) + m\pi)/l$ with $w = 0, 1, 2, \ldots, 2l - 1$. Figure 4 plots the structure of C line singularities of the theoretical vector field for the experimental result shown in Fig. 2. It can be seen that the left-handed and right-handed C lines, respectively, form two families of singular lines on the hyperboloid of revolution of one sheet. One interesting and important feature is that every singular line of one-handed family intersects every singular line of the other handed family, but any two singular lines of the same handed family are mutually skew. This finding can be explained by the fact that C points of opposite handedness cannot annihilate because the underlying vortices, which are in orthogonal, independent, field components, cannot annihilate. On the other hand, the peripheral C lines can be found to have the same winding number of $1/2$. This result is deeply related to the finding that the singularity structure is generally invariant upon propagation because C points with the same handedness and the same signed winding number numbers cannot annihilate. This finding is also relevant to the result of vortex trajectories in Gaussian beams obtained by Indebetouw [16] who found that when the vortices have all the same charge, the array remains invariant within the host beam. The L singularities can be determined by the conditions $|E_R|^2 = |E_L|^2$. With Eqs. (4) and (5), it can be found that there are $4l$ L surfaces on the $\rho - z$ plane with the azimuthal angles at where $\phi_n = n\pi/(2l)$, $n = 0, 1, 2, \ldots, 4l - 1$. From the loci of C lines, it can be confirmed that L surfaces separate regions of right-handed and left-handed polarization.

Another intriguing and important feature is that the experimental 3D polarization vector fields at the beam waist ($z = 0$) are made up of two linearly polarized modes with different spatial structures. For the case of $p = 0$, the experimental vector field at the beam waist can be given by $|E\rangle = E_x(\rho, \phi, 0)|x\rangle + E_y(\rho, \phi, 0)|y\rangle$, where

$$E_x(\rho, \phi, 0) = \sqrt{2}\Phi_{0,l-1,s}(\rho, 0)\{\tilde{\rho}_l^2 \cos[(l+1)\phi] - \cos[(l-1)\phi]\} \quad (6)$$

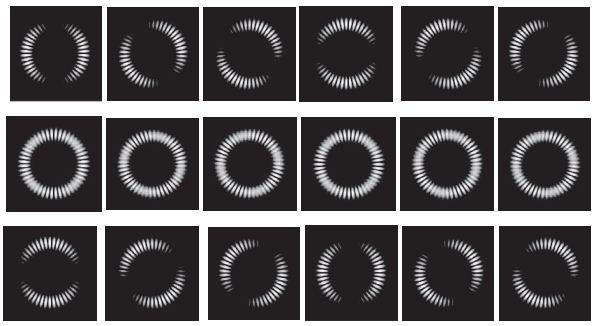

FIG. 3. Numerically reconstructed patterns for the experimental results shown in Fig. 2.

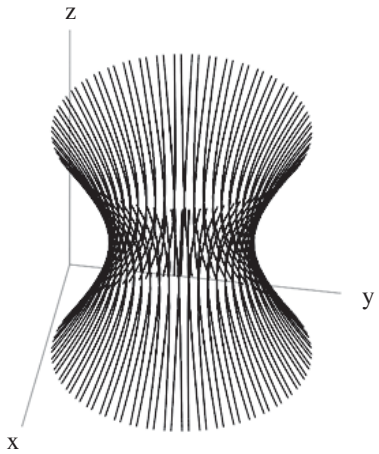

FIG. 4. Structure of the C line singularities of the theoretical vector field in the range of $-1.5z_R \le z \le 1.5z_R$ for the experimental mode shown in Fig. 2.

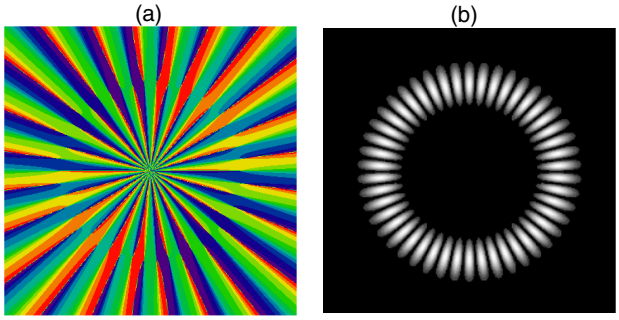

FIG. 5 (color online). (a) Numerical pattern of the angle function $\Theta(x, y) = \arctan(E_y/E_x)$ at the beam waist for the experimental mode shown in Fig. 2. (b) Numerical pattern of the correspondent intensity distribution.

and

$$E_y(\rho, \phi, 0) = \sqrt{2}\Phi_{0,l-1,s}(\rho, 0)\{\tilde{\rho}_l^2 \sin[(l+1)\phi] + \sin[(l-1)\phi]\}. \quad (7)$$

The transverse vector field at $z = 0$ can be verified to possess the V point singularities that are generally described in terms of the field of the angle function $\Theta(x, y) = \arctan(E_y/E_x)$ [17]. The vortices of $\Theta(x, y)$ are the V point singularities at which the orientation of the electric vector is undefined. Figure 5 depicts the angle pattern corresponding to the experimental result shown in Fig. 2. With Eqs. (6) and (7) and some algebra, it can be found that in addition to the central singularity at the origin, there are $2l$ peripheral V points symmetrically arrayed on a circle of radius $\rho_0 = \sqrt{\sqrt{l(l+1)}w_0/\sqrt{2}}$ at angles $\phi_m = m\pi/l$ with $m = 0, 1, 2, \ldots, 2l-1$. The loci of the V points are right at the intersections of the right-handed and left-handed C lines. In the far field, the Gouy phase plays a role to transform the V singularities to the C singularities. For the far-field $z \to \infty$, it can be also found that there are $2l$ peripheral V points symmetrically arrayed on a circle of radius $\rho_0 = \sqrt{\sqrt{l(l+1)}w(z)/\sqrt{2}}$ at angles $\phi_m = (2m+1)\pi/(2l)$ with $m = 0, 1, 2, \ldots, 2l-1$. Intriguingly, the combination of two different handed C singularities in the far field brings about the generation of the V point singularity. Each peripheral V point with the winding number of 1 is transformed to two different handed C points with the winding number of $1/2$. Manifestly, the winding numbers are conserved under propagation and during transformations [16].

In summary, we have used an isotropic microchip laser with the longitudinal-transverse coupling and the entanglement of the polarization states to generate the propagation-dependent polarization vector fields. In terms of the orthogonal circularly polarized vortex modes, we analytically reconstructed the experimental 3D coherent vector fields and found that each circular polarized component is made up of two Laguerre-Gaussian (LG) modes with different topological charges. We employed the analytical representation to perform comprehensive analysis for the singularities of the C lines, L surfaces, and V points. It was found that the C line singularities form a hyperboloidal structure and the V point singularities are right at the intersections of two different handed C lines.

The authors thank the National Science Council for their financial support of this research under Contract No. NSC-94-2112-M-009-034. This work is also supported in part by the MOE-ATU project.

*Current address: Department of Electrophysics, National Chiao Tung University, 1001 TA Hsueh Road, Hsinchu Taiwan, 30050.
Email address: yfchen@cc.nctu.edu.tw

[1] *Optical Vortices*, edited by M. V. Vasnetsov and K. Staliunas (Nova Science, New York, 1999).
[2] M. S. Soskin and M. V. Vasnetsov, in *Progress in Optics*, edited by E. Wolf (Elsevier, New York, 2001), Vol. 42, Chap. 4.
[3] P. Seba, U. Kuhl, M. Barth, and H. J. Stockmann, J. Phys. A **32**, 8225 (1999).
[4] V. R. Misko, V. M. Fomin, J. T. Devreese, and V. V. Moshchalkov, Phys. Rev. Lett. **90**, 147003 (2003).
[5] K. W. Madison, F. Chevy, W. Wohlleben, and J. Dalibard, Phys. Rev. Lett. **84**, 806 (2000).
[6] K. F. Berggren, A. F. Sadreev, and A. A. Starikov, Phys. Rev. E **66**, 016218 (2002).
[7] P. G. de Gennes and J. Prost, *The Physics of Liquid Crystals* (Oxford University Press, New York, 1993), 2nd ed.
[8] J. F. Nye, Proc. R. Soc. A **387**, 105 (1983); M. Soskin, V. Denisenko, and R. Egorov, J. Opt. A Pure Appl. Opt. **6**, S281 (2004); M. V. Berry, J. Opt. A Pure Appl. Opt. **6**, 475 (2004).
[9] J. F. Nye, *Natural Focusing and Fine Structure of Light: Caustics and Wave Dislocations* (Institute of Physics Publishing, Bristol, 1999).
[10] M. V. Berry, J. Opt. A Pure Appl. Opt. **6**, 475 (2004).
[11] M. S. Soskin, V. Denisenko, and I. Freund, Opt. Lett. **28**, 1475 (2003); F. Flossmann, U. T. Schwartz, M. Maier, and M. R. Dennis, Phys. Rev. Lett. **95**, 253901 (2005); A. Volyar, V. Shvedov, T. Fadeyeva, A. S. Desyatnikov, D. N. Neshev, W. Krolikowski, and Y. S. Kivshar, Opt. Express **14**, 3724 (2006).
[12] F. Prati, G. Tissoni, M. S. Miguel, and N. B. Abraham, Opt. Commun. **143**, 133 (1997).
[13] Y. F. Chen, T. H. Lu, and K. F. Huang, Phys. Rev. Lett. **96**, 033901 (2006).
[14] Y. F. Chen, T. H. Lu, K. W. Su, and K. F. Huang, Phys. Rev. Lett. **96**, 213902 (2006).
[15] A. N. Alexeyev, T. A. Fadeyeva, A. V. Volyar, and M. S. Soskin, Semicond. Phys. Quantum Electron. Optoelectron. **1**, 82 (1998); P. Z. Dashti, F. Alhassen, and H. P. Lee, Phys. Rev. Lett. **96**, 043604 (2006).
[16] G. Indebetouw, J. Mod. Opt. **40**, 73 (1993).
[17] I. Freund, Opt. Commun. **199**, 47 (2001); **201**, 251 (2002).